

# Structure and Properties of Ti-19.7Nb-5.8Ta Shape Memory Alloy Subjected to Thermomechanical Processing Including Aging

S. Dubinskiy, Vladimir Brailovski, S. Prokoshkin, V. Pushin, K. Inaekyan, V. Sheremetyev, M. Petrzhik, and M. Filonov

(Submitted January 23, 2013; in revised form March 27, 2013; published online April 16, 2013)

In this work, the ternary Ti-19.7Nb-5.8Ta (at.%) alloy for biomedical applications was studied. The ingot was manufactured by vacuum arc melting with a consumable electrode and then subjected to hot forging. Specimens were cut from the ingot and processed by cold rolling with  $e = 0.37$  of logarithmic thickness reduction and post-deformation annealing (PDA) between 400 and 750 °C (1 h). Selected samples were subjected to aging at 300 °C (10 min to 3 h). The influence of the thermomechanical processing on the alloy's structure, phase composition, and mechanical and functional properties was studied. It was shown that thermomechanical processing leads to the formation of a nanosubgrained structure (polygonized with subgrains below 100 nm) in the 500–600 °C PDA range, which transforms to a recrystallized structure of  $\beta$ -phase when PDA temperature increases. Simultaneously, the phase composition and the  $\beta \rightarrow \alpha'$  transformation kinetics vary. It was found that after conventional cold rolling and PDA, Ti-Nb-Ta alloy manifests superelastic and shape memory behaviors. During aging at 300 °C (1 h), an important quantity of randomly scattered equiaxed  $\omega$ -precipitates forms, which results in improved superelastic cyclic properties. On the other hand, aging at 300 °C (3 h) changes the  $\omega$ -precipitates' particle morphology from equiaxed to elongated and leads to their coarsening, which negatively affects the superelastic and shape memory functional properties of Ti-Nb-Ta alloy.

**Keywords** biomaterials, electron microscopy, heat treating, mechanical testing, rolling, titanium

## 1. Introduction

Ti-based alloys have been recognized for many years as excellent materials for biomedical implants mainly because of their low density, high corrosion resistance, and biocompatibility combined with low Young's modulus (Ref 1-3). Based on the formation of stable ( $\alpha$ ,  $\alpha + \beta$ ) and metastable ( $\beta$ ) phases in these alloys, a wide variety of mechanical properties mimicking those of biological tissues (e.g., superelasticity) can be obtained. This is the main reason behind significant interest in novel titanium metastable alloys containing exclusively biocompatible elements, such as Nb, Ta, Zr, or Mo (Ref 4, 5).

S. Dubinskiy, École de technologie supérieure, 1100, Notre-Dame Street West, Montreal, QC H3C 1K3, Canada; and National University of Science and Technology "MISIS", 4, Leninsky prosp., Moscow 119049, Russian Federation; Vladimir Brailovski and K. Inaekyan, École de technologie supérieure, 1100, Notre-Dame Street West, Montreal, QC H3C 1K3, Canada; S. Prokoshkin, V. Sheremetyev, M. Petrzhik, and M. Filonov, National University of Science and Technology "MISIS", 4, Leninsky prosp., Moscow 119049, Russian Federation; and V. Pushin, Institute of the Metals Physics, Ural Branch of the Russian Academy of Sciences, 18, Sofia Kovalevskaya Street, Ekaterinburg 620990, Russian Federation. Contact e-mail: vladimir.brailovski@etsmtl.ca.

Given that tantalum and niobium are considered as the strongest beta-stabilizing biocompatible metals, ternary or quaternary Ti-Nb-based shape memory alloys are being widely studied (Ref 6-8). The structure and properties of these alloys depend on a complex sequence of phase transformations, which are influenced by thermomechanical processing conditions, such as severity of plastic deformation, post-deformation annealing (PDA) temperature, and cooling rate (Ref 9, 10). In this work, Ti-19.7Nb-5.8Ta (at.%) shape memory alloy samples subjected to thermomechanical processing including cold rolling (CR), PDA, and aging (AG) are characterized by TEM and x-ray diffraction techniques, microhardness, single- and multi-cycle isothermal tensile testing, and strain/stress recovery measurement techniques.

## 2. Experimental Procedure

### 2.1 Casting

Ti-Nb-Ta ingots were cast by vacuum arc melting with a consumable electrode in a "VDP-0.02" furnace. The electrode was made from bars of pure Ti and Nb-Ta master alloy. Hot forging of the 7-kg, 80-mm-diameter ingot was carried out at 900–950 °C in air. As a result, a 51-mm-diameter cylinder was obtained. The surface layer of the cylinder was removed by machining the cylinder to 50 mm diameter. Chemical analysis performed after this treatment across the cylinder cross section showed that the impurities' content (including oxygen) corresponded to grade 1, ASTM F67-00 (see Table 1). For a subsequent study, the ingot was cut into 8-mm-thick disks, and

**Table 1 Ti-Nb-Ta ingot composition**

Element	wt. %	at. %
Ti	55.4	74.5
Nb	28.4	19.7
Ta	16.2	5.8
O	0.039 ± 0.008	...
N	0.0075 ± 0.0021	...
H	0.00556 ± 0.00087	...
C	0.009 ± 0.002	...

then into 2-mm-thick—30–50-mm long plates. Based on the data of Table 1, the  $M_s$  temperature was estimated as being close to +50 °C (Ref 7).

## 2.2 Thermomechanical Processing

After four-pass cold rolling to logarithmic thickness reduction of  $e = 0.37$ , Ti-Nb-Ta plates were EDM cut to form  $1 \times 1.5 \times 50$  (mm) specimens and subjected to PDA at 400, 450, 500, 550, 600, 650, 700, and 750 °C (all 1 h) followed by water quenching to room temperature (RT). After PDA at 500 °C (1 h), aging at 300 °C for various times (10 min, 30 min, 1 h, and 3 h) was performed to estimate the effect of  $\omega$ -phase precipitation on the functional properties of the studied alloy.

## 3. Experimental Methods

The effect of thermomechanical processing on the microstructure and functional (shape memory) properties of Ti-Nb-Ta alloy was studied using the following TEM and x-ray diffraction analyses and mechanical and thermomechanical testing routines.

- *TEM analysis* of selected samples subjected to CR ( $e = 0.37$ ) + PDA (500, 600, 650, and 750 °C, all 1 h) and CR ( $e = 0.37$ ) + PDA ( $T = 500$  °C, 1 h) + aging at 300 °C (1 and 3 h) was carried out using “JEOL 2100CX” transmission electron microscope. Thin foils for TEM were prepared from 0.1-mm-thick platelets by electropolishing at -38 °C using 15% HNO<sub>3</sub> spirit solution and “TENUPOL-5” equipment (Struers, Denmark).
- *X-ray diffraction phase analysis* of selected samples subjected to CR ( $e = 0.37$ ) + PDA (500, 600, and 750 °C, all 1 h) and CR ( $e = 0.37$ ) + PDA ( $T = 500$  °C, 1 h) + aging at 300 °C (1 and 3 h) was performed using an “Ultima IV Rigaku” diffractometer (monochromatic CuK $\alpha$ -radiation). The samples for x-ray analysis were mechanically polished and chemically etched using an acid solution of the following composition: 2HF:1HNO<sub>3</sub>:17H<sub>2</sub>O.
- *Microhardness measurements* were performed using an “INSTRON Wilson Tukon 2100” (500 g, 10 s) instrument; five HV measurements were performed for each thermomechanical processing condition, and mean and standard deviation values were calculated.
- *Single- and multi-cycle isothermal tensile testing* was carried out at RT and at 40 °C using an “MTS Mini Bionix” system. Single-cycle testing consisted of loading up to 2% of strain and then unloading down to zero load with strain rate of 0.002 s<sup>-1</sup>. During multi-cycle testing, a constant strain of  $\epsilon_t = 2\%$  was applied in each cycle to specimen

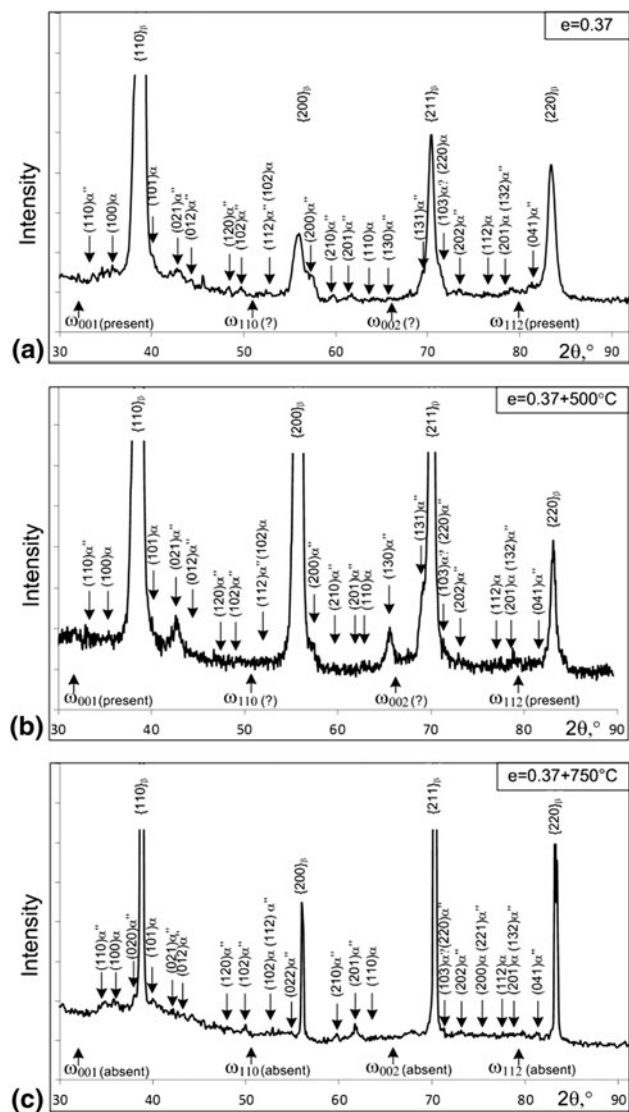


**Fig. 1** X-ray diffractograms of Ti-Nb-Ta alloy subjected to CR  $e = 0.37$  (a),  $e = 0.37$  + PDA ( $T = 500$  °C, 1 h) (b), and  $e = 0.37$  + PDA ( $T = 750$  °C, 1 h) (c); “↑” expected locations of  $\omega$ -phase x-ray lines

failure. The number of cycles to failure was measured, and the characteristic features of a superelastic loop, such as transformation yield stress  $\sigma_{tr}^A \rightarrow M$ , Young’s modulus, and accumulated strain, were identified.

- *Constant-strain temperature scanning* was performed on selected samples using a LAMSI tensile testing bench. The samples subjected to CR ( $e = 0.37$ ) + PDA ( $T = 450, 500, 600,$  and  $700$  °C, all 1 h) and CR ( $e = 0.37$ ) + PDA ( $T = 500$  °C, 1 h) + AG at 300 °C (1 h and 3 h) were cooled down to -150 °C, then stretched to a 2.5% strain, fixed, heated up to 200 °C, and cooled back to -150 °C. The recovery stress generation-relaxation diagrams during heating and cooling were plotted.
- *Shape recovery testing* was carried out on selected samples after  $e = 0.37$  + PDA ( $T = 450, 500, 600, 700$  °C, 1 h) as well as after CR ( $e = 0.37$ ) + PDA ( $T = 500$  °C, 1 h) + AG at 300 °C (1 and 3 h). The samples were bent at -196 °C around cylindrical mandrels of different radii and heated up by hot air to a complete shape recovery. The

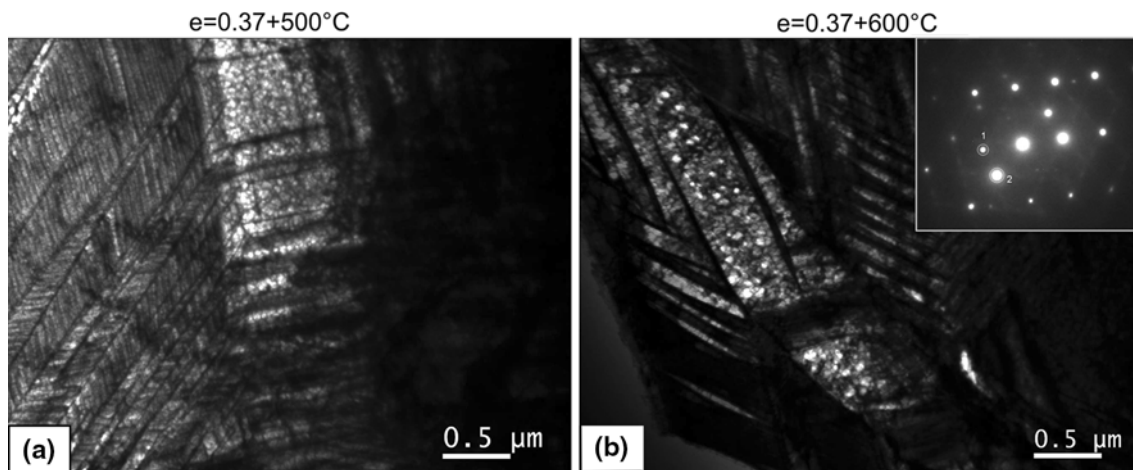


**Fig. 2** Structure of Ti-Nb-Ta alloy subjected to CR ( $e = 0.37$ ) + PDA [ $T = 500$  (a) and  $600$  °C (b); 1 h]; (a) bright field image, (b) dark-field image in a  $\beta$ -phase matrix reflection and SAED pattern ( $\langle 110 \rangle_{\beta}$  zone axis with two high-angle misorientations)

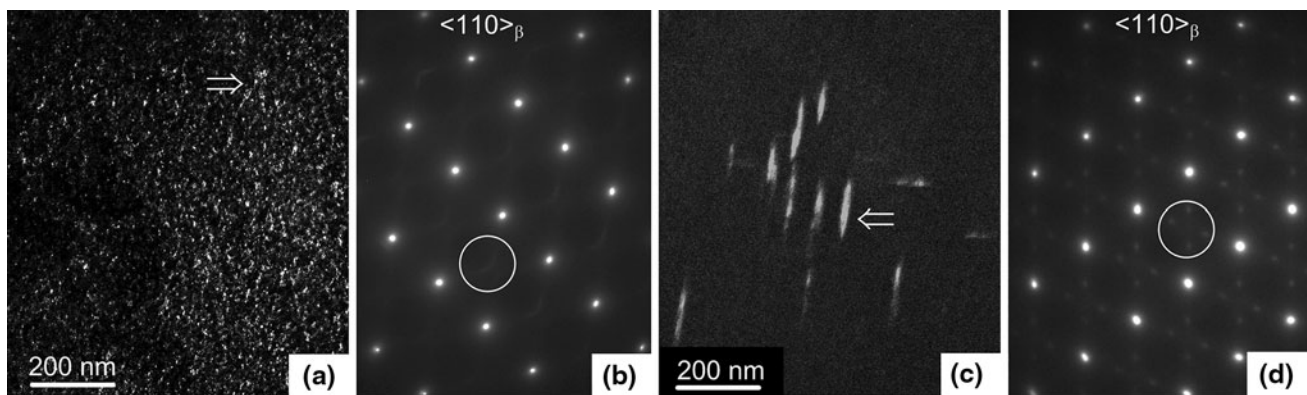


**Fig. 3** Dark-field image in  $\omega$ -phase reflections of Ti-Nb-Ta alloy after CR ( $e = 0.37$ ) + PDA ( $T = 500$  °C, 1 h) + AG [ $T = 300$  °C, 1 h (a) and 3 h (c)], and corresponding SAED pattern,  $\langle 110 \rangle_{\beta}$  zone axis (b, d). Doubled arrow indicates an elongated row of  $\omega$  particles

shape memory (SM) recovery strain  $\varepsilon_r$  was measured as a function of initial (induced) strain  $\varepsilon_i$ , and maximum completely SM-recoverable strain  $\varepsilon_{r,1}^{\max}$  was then determined with 0.15% tolerance.

## 4. Results

### 4.1 Structure of Thermomechanically Treated Ti-Nb-Ta Alloy

As seen in Fig. 1(a), the main phase in Ti-Nb-Ta alloy after conventional cold rolling is  $\beta$ -phase, whereas  $\alpha''$ ,  $\omega$ , and possibly  $\alpha$  phases are present in small quantities. A parallel electron microscopy study shows that the  $\beta$ -phase contains high dislocation density. PDA initiates the recovery, polygonization, and recrystallization processes in  $\beta$ -phase, which is confirmed by the continuous narrowing of the  $\beta$ -phase x-ray lines as PDA temperature increases up to  $750$  °C (Fig. 1b, c). This phase composition at RT does not change significantly after PDA at

$500$  °C; however, the  $\alpha''$ -phase content is distinctly higher than that of  $\omega$ - and  $\alpha$ -phases (the presence of the latter is not evident) (Fig. 1b). PDA at  $750$  °C reveals the presence of additional  $\alpha''$ - and  $\alpha$ -phases and the absence of  $\omega$ -phase (Fig. 1c).

A TEM study after PDA at  $500$  and  $600$  °C reveals a nanosubgrained (NS) dislocation substructure of  $\beta$ -phase (subgrain size below  $100$  nm) with “imposed”  $\alpha''$ -martensite crystals (Fig. 2a, b). The  $\alpha''$ -martensite manifests a typical packet-like morphology of pairly twinned martensite crystals. The  $\alpha''$  crystals inherit the NS structure from the  $\beta$ -phase. Note that a significant  $\alpha''$ -martensite quantity at RT may be partially caused by additional  $\alpha''$  formation during low-temperature electropolishing of thin foils. Increasing the PDA temperature above  $600$  °C leads to  $\beta$ -phase recrystallization, and PDA at  $750$  °C results in  $\beta$ -phase grain growth up to  $20$ - $30$   $\mu\text{m}$  with some quantity of  $\alpha$ - and  $\alpha''$ -phases, but without  $\omega$ -phase (Fig. 1c).

Even though x-ray diffraction analysis of the aged after  $500$  °C PDA samples ( $300$  °C, 10 min to 3 h) does not point to significant variations in the phase composition, TEM makes it possible to reveal the following changes in the  $\omega$ -phase structure. After  $300$  °C (1 h) aging, very fine ( $d = 5$ - $10$  nm)



**Table 2 Phase constituents and other microstructural features resulting from TMTs**

PDA and AG after CR $e = 0.3$	Structure of $\beta$ -phase	Other phases in presence
PDA 500 °C (1 h) and 600 °C (1 h)	Nanosubgrained (NS) dislocation substructure with subgrain size less than 100 nm	$\alpha''$ -Martensite with typical packet-like morphology of pairly twinned martensite crystals; $\alpha''$ crystals inherit the b-phase NS substructure; x-phase is identified only by TEM
PDA 750 °C (1 h)	Recrystallized structure with grain size of about 20-30 $\mu\text{m}$	Some quantity of $\alpha'$ - and $\alpha$ -phases, but without x-phase; $\alpha''$ crystals inherit the b-phase NS substructure
PDA 500 °C (1 h) + AG 300 °C (1 h)	Nanosubgrained (NS) dislocation substructure with subgrain size less than 100 nm	Very fine ( $d = 5\text{-}10\text{ nm}$ ) randomly scattered equiaxed $\omega$ -phase particles
PDA 500 °C (1 h) + AG 300 °C (3 h)		$\omega$ -reflections' system becomes more distinct; formation of elongated rows (up to 100-150 nm long—30 nm wide) of coarsened ( $d = 20\text{-}30\text{ nm}$ ) $\omega$ -phase particles

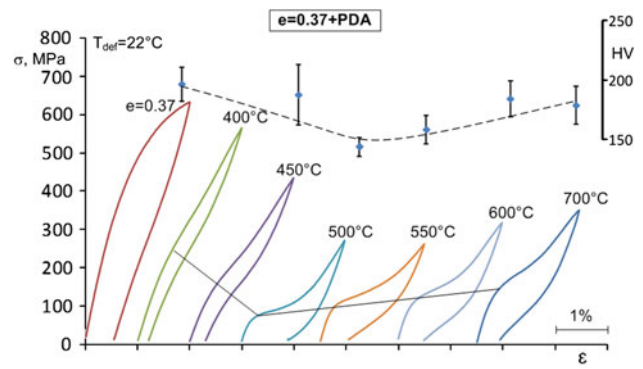


**Fig. 4** Microhardness Vickers measurements and stress-strain diagrams of Ti-Nb-Ta alloy subjected to CR ( $e = 0.37$ ) + PDA (1 h) at different temperatures

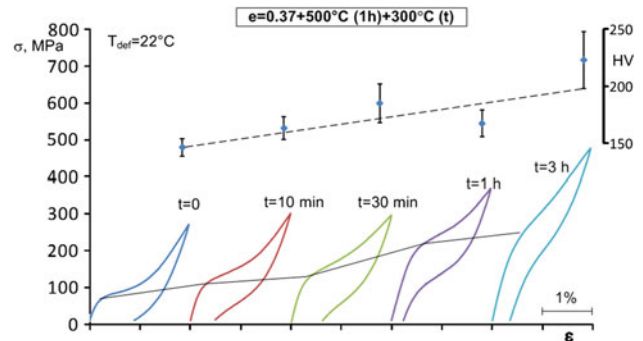


**Fig. 5** Microhardness Vickers measurements and stress-strain diagrams of Ti-Nb-Ta alloy subjected to CR ( $e = 0.37$ ) + PDA ( $T = 500\text{ °C}$ , 1 h) + AG at  $300\text{ °C}$  with different aging times ( $t$ )

randomly scattered equiaxed  $\omega$ -phase particles manifest a weak tendency to form elongated rows, as shown in the dark-field image (Fig. 3a) obtained from a group of very weak  $\omega$  diffuse reflections in positions close to “1/3”  $\langle 112 \rangle_{\beta}$  and “2/3”  $\langle 111 \rangle_{\beta}$  (Fig. 3b). After  $300\text{ °C}$  (3 h) aging, the system of  $\omega$ -reflections becomes more distinct (Fig. 3d), and the tendency to form elongated rows of coarsened  $\omega$  particles is enhanced (Fig. 3c). This morphology cannot be attributed to  $\alpha$ -phase crystals because  $\alpha$ -phase reflections are absent in the corresponding SAED pattern (Fig. 3d).

Table 2 resumes the correlation between the thermomechanical treatment and microstructure of Ti-Nb-Ta alloy.

#### 4.2 Microhardness and Single-Cycle Tensile Testing

The results of RT microhardness and tensile testing of Ti-Nb-Ta alloy are presented in Fig. 4 and 5. As confirmed by microhardness measurements and stress-strain diagrams (Fig. 4), Ti-Nb-Ta alloy subjected to conventional cold rolling manifests a net softening after PDA at  $500\text{-}550\text{ °C}$  (1 h). The shape of the loading-unloading diagrams after PDA in that temperature range is typical for shape memory behavior with a certain contribution of superelasticity (Ref 11). In contrast, stress-strain diagrams after PDA at  $400\text{-}450$  and  $600\text{ °C}$  manifest preferentially superelastic behavior. Furthermore, additional aging at  $300\text{ °C}$  after PDA at  $500\text{ °C}$  (1 h) leads to appreciable changes in mechanical behavior: The greater the aging time, the higher the alloy strengthening and the closer the

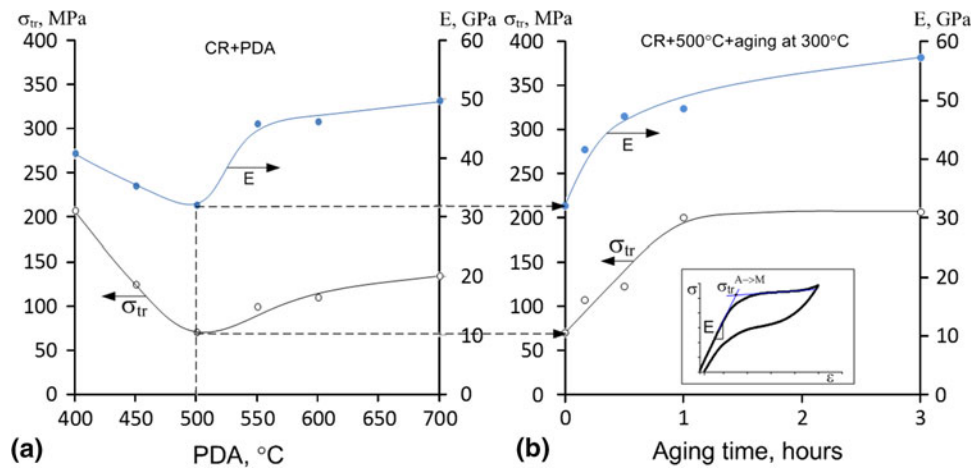


**Fig. 6** Transformation yield stress ( $\sigma_{tr}$ ) and Young's modulus of Ti-Nb-Ta alloy subjected to (a)  $e = 0.37 + \text{PDA}$  (1 h) at different temperatures and (b)  $e = 0.37 + \text{PDA}$  ( $T = 500^\circ\text{C}$ , 1 h) + AG ( $300^\circ\text{C}$ , 10 min to 3 h). Inset: schematic presentation of the transformation yield stress and Young's modulus measurements

alloy's behavior comes to perfect superelasticity; the latter is valid up to a certain limit, the best fit corresponding to 1-h aging (Fig. 5). To sum up these results, Fig. 6 illustrates the evolution of Young's modulus ( $E$ ) and transformation yield stress ( $\sigma_{tr}$ ) as a function of the annealing temperature and aging time.

#### 4.3 Multi-Cycle Tensile Testing

In Fig. 7, multi-cycle stress-strain diagrams obtained after different processing routes are collected. A distinct cyclic behavior close to linear superelasticity is observed for low-temperature annealing: 400 and 450 °C (Fig. 7b, c). The accumulated strain to failure in these cases is the lowest—below 3%—as compared to 6.5% after annealing at 700 °C (Fig. 7g). After aging at 300 °C of the sample annealed at 500 °C, simultaneous improvement of superelastic behavior and cyclic life is observed, the maximum corresponding to 1-h aging time (Fig. 7h-j).

Comparative tensile cycling at RT and at 40 °C was performed using the specimens subjected to annealing at 600 °C for 1 h (Fig. 8). It can be observed that, according to the Clausius-Clapeyron relationship, the higher the testing temperature, the higher the transformation yield stress:  $\Delta\sigma/\Delta T \approx 2.5 \pm 1.0 \text{ MPa}/^\circ\text{C}$ . This transformation yield stress-temperature slope value is close to those observed for similar alloys in Ref 7, 12. That supports the assertion that we truly deal with stress-induced thermoelastic martensitic transformation.

#### 4.4 Thermomechanical Testing

**4.4.1 Recovery Stress Testing.** The results of the constant-strain temperature scanning experiment presented in Fig. 9(a) illustrate the influence of the PDA temperature on the recovery stress generation and therefore on the reverse martensitic transformation temperature range under stress. The maximum recovery stresses  $\sigma_r^{\max} = \sigma^{A_r^\sigma} - \sigma^{A_s^\sigma}$  correspond to annealing at 600 and 500 °C and are equal to 80 and 50 MPa, respectively. The effect of the PDA temperature on the characteristic stresses of the generation-relaxation curves,  $\sigma^{A_r^\sigma}$ ,  $\sigma^{A_s^\sigma}$  (Fig. 10a), is similar to the evolution of the transformation yield stress and Young's modulus shown in

Fig. 6(a). The initial lowering of stress upon heating is due to thermal dilatation of the specimen followed by recovery stress generation caused by constrained  $\alpha'' \rightarrow \beta$  martensitic transformation.

Stress-temperature diagrams of the samples subjected to aging at 300 °C (1 and 3 h) after CR + 500 °C (1 h) reflect a certain evolution in material microstructure (Fig. 9b) as compared to the non-aged specimens (Fig. 9a). After 1-h aging, the stress-temperature diagram shows a distinct stress generation, whereas 3-h aging suppresses the martensitic transformation and, therefore, stress generation becomes very weak (Fig. 9b, 10b).

**4.4.2 Recovery Strain Testing.** For Ti-19.7Nb-5.8Ta alloy, the completely recoverable shape memory strain in bending after stress-free heating from  $-196^\circ\text{C}$  ( $\epsilon_{r,1}^{\max}$ ) reaches its maxima of about 1.5-2% after annealing in the 500-700 °C range and about 1% after 400-450 °C annealing (Fig. 11a). Aging at 300 °C after  $e = 0.37 + \text{PDA}$  ( $T = 500^\circ\text{C}$ , 1 h) (Fig. 11b) results in a net decrease ( $\epsilon_{r,1}^{\max}$  under 1%) in shape restoration upon heating.

Figure 11 presents the recovery strain of the shape memory effect (SME) only. This experiment was realized in three consecutive steps: deformation at low temperature, unloading at low temperature, and heating. Induced strain was measured after unloading at  $-196^\circ\text{C}$ ; thus, elastic + superelastic recovery strains were excluded from consideration. Recovery strain due to SME was measured upon heating. Intensive precipitation hardening during aging was accompanied by an increase in the alloy's true and transformation yield stresses. Thus, to induce SME, it was necessary to apply higher stresses close to the alloy's true yield stress, which led to accumulation of residual strain and, therefore, to decrease in recoverable strain.

## 5. Discussion

It can be shown that the measured mechanical and functional properties of the studied alloy are in direct correlation with the material microstructure. PDA of the Ti-Nb-Ta SMA initiates the recovery, polygonization, and recrystallization processes in

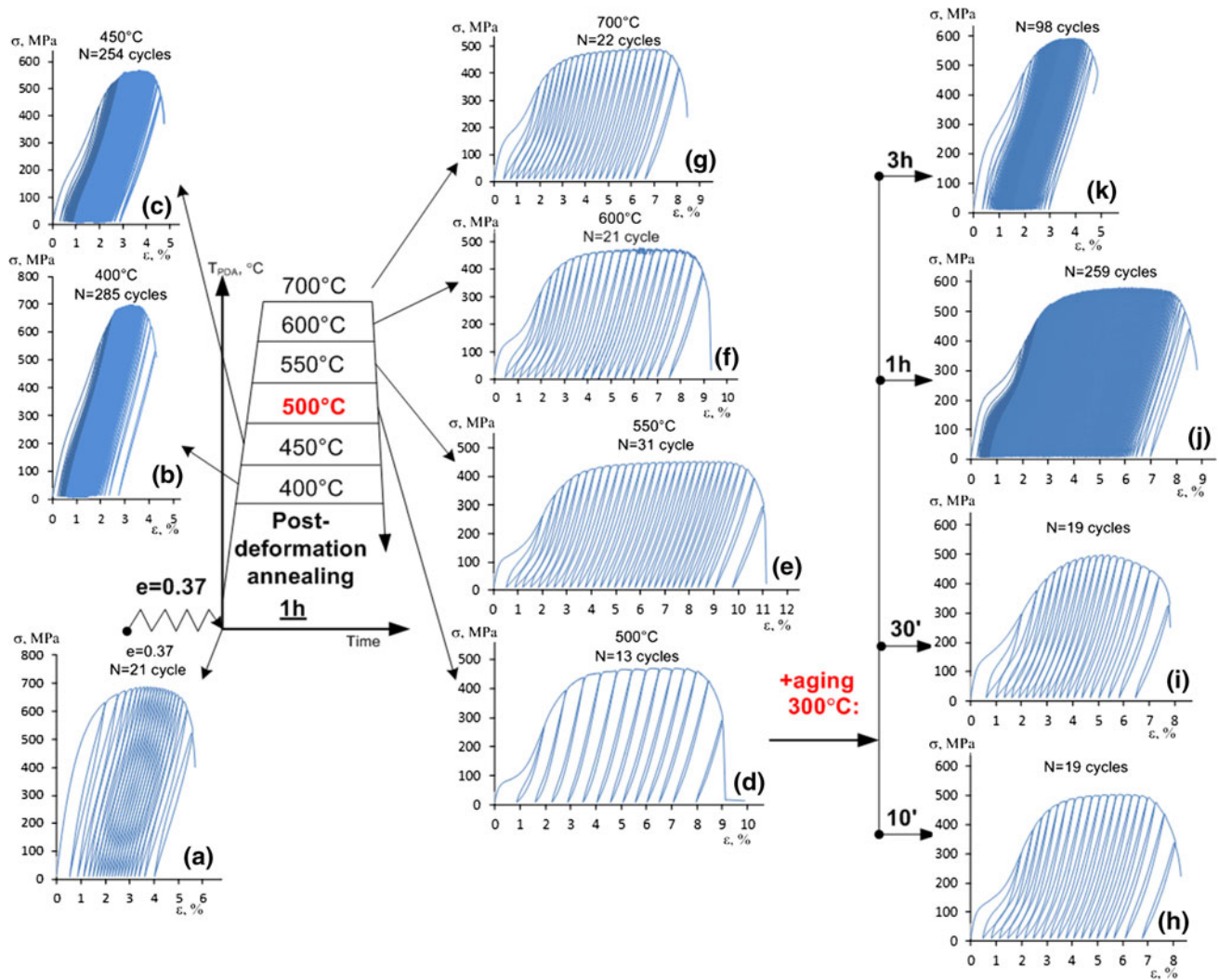


**Fig. 7** Stress-strain cycling diagrams of Ti-Nb-Ta alloys after  $e = 0.37 + \text{PDA}$ : (a) as-deformed,  $e = 0.37$ ; deformed and annealed at 400 (b); 450 (c); 500 (d); 550 (e); 600 (f); and 700 °C (g) (all 1 h). Aged at 300 °C after  $e = 0.37 + 500$  °C (1 h): 10 min (h); 30 min (i); 1 h (j); and 3 h (k)

$\beta$ -phase (Fig. 1, 2). Low-temperature aging of the NS structure at 300 °C is accompanied by a slow development of the  $\omega$ -phase precipitation in the nanosubgrained  $\beta$ -phase. The  $\omega$ -particles preserve their globular shape, random distribution, and very fine size for up to 1 h of aging (Fig. 3), thus creating an optimum dispersion hardening for the longest cyclic life. During further aging, a transformation to elongated coarsened  $\omega$ -particles develops (Fig. 3). As a result, this “overaging” worsens superelastic cyclic life.

Annealing at 500 °C corresponds to drastic material softening, which is clearly observed in both single-cycle (Fig. 4) and multi-cycle (Fig. 7 a-d) testing. On one hand, the higher the annealing temperature, the lower the dislocation density and therefore the higher the alloy’s  $M_s$  temperature (Ref 9). On the contrary, the higher the annealing temperature, the higher the enrichment of  $\beta$ -phase by Nb and Ta  $\beta$ -stabilizers because of the formation of  $\omega$ - and  $\alpha''$ -phases with higher than  $\beta$ -phase Ti content, and therefore the lower the alloy’s  $M_s$  temperature (Ref 13). These phenomena concurrently influence the alloy’s mechanical behavior: The closer the testing temperature to  $M_s$  temperature, the lower the phase transformation stress (Ref 14).

In the vicinity of 500 °C, concurrence of the above-mentioned phenomena is superimposed on the low stability of  $\beta$ -phase ( $\beta \rightarrow \alpha''$  transformation) and therefore results in accentuated material softening. When annealing temperature approaches 700 °C, material recrystallization results in a significant grain refinement of the studied alloy (Ref 15), which additionally contributes to the material hardening.

The greater the aging time, the higher the transformation yield stress of the material (Fig. 5, 7 h-k). These observations are explained by two concomitant phenomena: the enrichment of the parent phase by Nb and Ta, and the  $\omega$ -phase precipitation hardening. The first assertion is based on the information known from Ref 10, whereas the second assertion is supported by a TEM study of the  $\omega$ -phase precipitation phenomenon presented in section 4.1 of this paper.

It can be seen that the following processing sequences—route (A), Fig. 7(b), (c):  $e = 0.37 + \text{PDA}$  ( $T = 400, 450$  °C, 1 h); and route (B), Fig. 7(j):  $e = 0.37 + \text{PDA}$  ( $T = 500$  °C, 1 h) + AG (300 °C, 1 h)—lead to the longest cyclic lives. However, the strain accumulated to failure is much larger after route (B) than after route (A). The reason for this difference



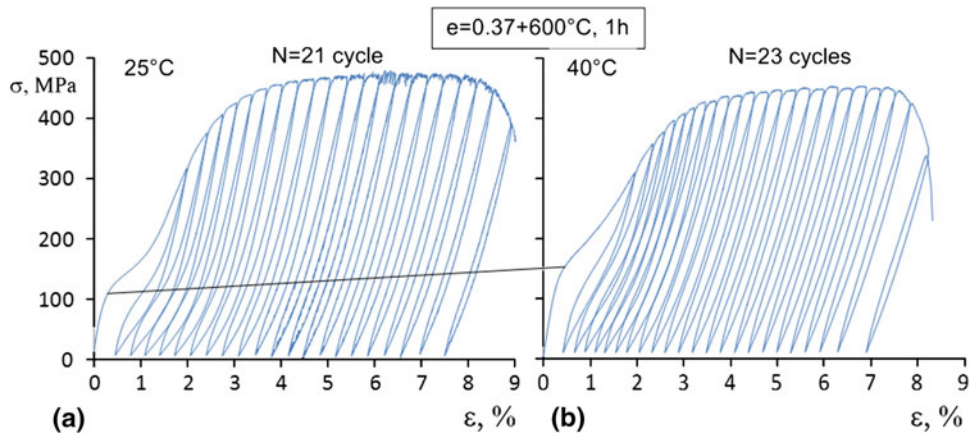


Fig. 8 Cycling stress-strain diagrams of Ti-Nb-Ta alloys after  $e = 0.37 + 600^\circ\text{C}$  at (a)  $25^\circ\text{C}$  and (b)  $40^\circ\text{C}$

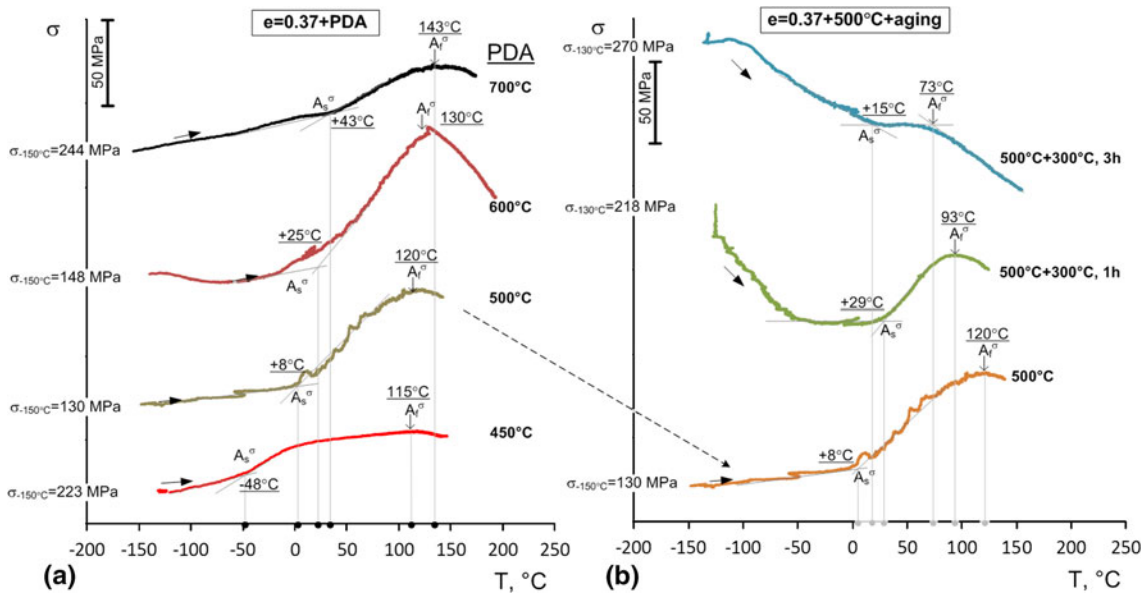


Fig. 9 Constant-strain temperature scanning diagrams for 2.5% strain for Ti-Nb-Ta subjected to  $e = 0.37 + \text{PDA}$  ( $T = 450, 500, 600,$  and  $700^\circ\text{C}$ ) (a) and  $e = 0.37 + 500^\circ\text{C}$  (1 h) + aging at  $300^\circ\text{C}$  (1 and 3 h) (b)

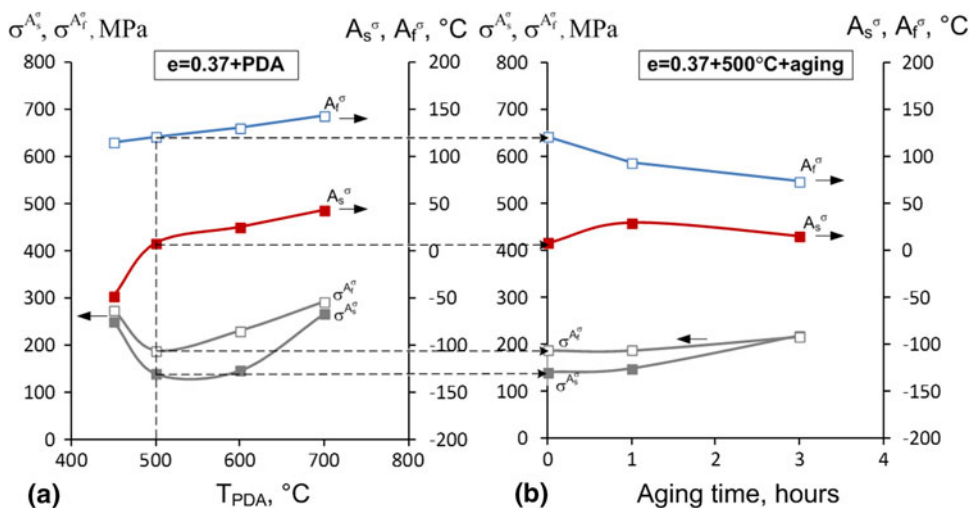
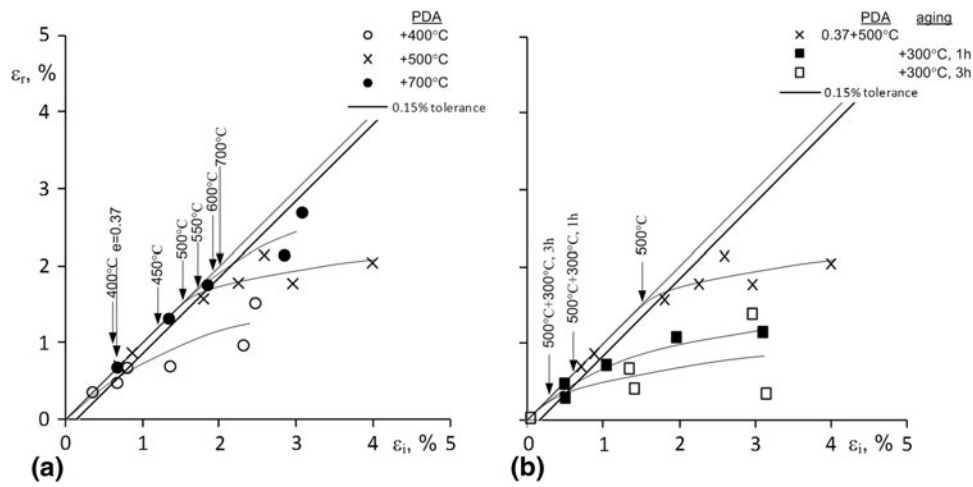
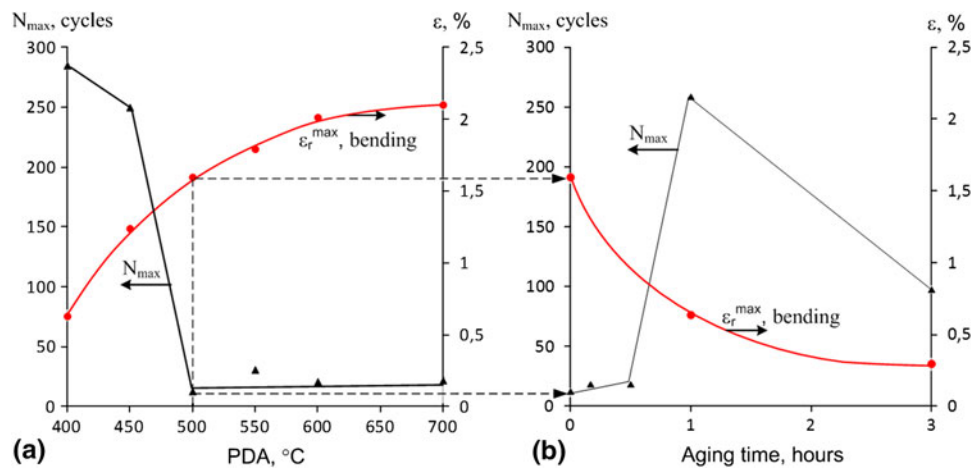


Fig. 10 Variation of the reverse martensitic transformation temperatures and characteristic stresses for Ti-Nb-Ta subjected to  $e = 0.37 + \text{PDA}$  (a) and  $e = 0.37 + 500^\circ\text{C}$  (1 h) + aging at  $300^\circ\text{C}$  (1 and 3 h) (b)



**Fig. 11** Recovery strain dependence on induced strain in bending SM testing at  $-196\text{ }^{\circ}\text{C}$  and subsequent heating above  $A_f$  of Ti-Nb-Ta alloy subjected to CR + PDA (1 h) (a) and CR + PDA + AG (300  $^{\circ}\text{C}$ , 1 and 3 h) (b). To facilitate observation, not all the experimental points are presented



**Fig. 12** Maximum completely recoverable strain of shape memory effect ( $\epsilon_r^{\max}$ ) and number of cycles to failure  $N_{\max}$  after  $e = 0.37 + \text{PDA}$  (a) and  $e = 0.37 + 500\text{ }^{\circ}\text{C}$  (1 h) +  $300\text{ }^{\circ}\text{C}$  ( $t = \text{var}$ ) (b)

resides in the quite different material microstructures resulting from these processing routes: Route (A) leads to a highly dislocation- and  $\omega$  precipitation-hardened structure, whereas route (B) leads to an  $\omega$ -precipitation-hardened NS structure, the latter being more ductile than the former. Indeed the true (“dislocation”) yield stresses  $\sigma_y$  are about 600 and 450 MPa for these two cases (Fig. 7c, f). When aging time increases from 1 to 3 h,  $\omega$ -phase particles change size, quantity, and distribution: They grow, their quantity increases, and distribution changes. From random distribution of small equiaxed particles, they now form large elongated rows of coarsened particles (Table 2), which naturally leads to excessive structure hardening and to a decrease in the crack’s propagation resistance under repetitive loading (Ref 13, 16). Figure 12 contains the quantitative analysis of the number of cycles to failure after different TMTs.

Given that the main objective of cyclic testing was to determine the most appropriate processing conditions from the functional fatigue point of view, the number of cycles to failure was by far the most important parameter to be discussed. For example, if we compare diagram (d) and diagram (j) of Fig. 7,

failure strain in both cases is about 9%, whereas the number of cycles to failure is very different, 13 and 259, respectively. Based on these observations, the processing conditions leading to diagram (j) are much better suited for cyclic application than the processing conditions leading to diagram (d). It should be noted that Ti-19.7Nb-5.8Ta (at.%) SMA of this study manifests significantly lower fatigue life than Ti-21.8Nb-6Zr (at.%), under similar sample preparation and testing conditions. For example, after  $e = 0.37 + \text{PDA}$  (600  $^{\circ}\text{C}$ , 30 min), the number of cycles to failure of Ti-Nb-Zr alloy is 877 (Ref 12), whereas it is only  $\sim 260$  in Ti-Nb-Ta alloy of this study. Note also that Ti-50.26 at.%Ni SMA outperforms from five to ten times any Ti-Nb-based alloys in this respect: The number of superelastic cycles to failure of Ti-Ni samples reaches 2700 (3% strain applied in each cycle) when the alloy’s microstructure corresponds to the mixed nanosubgrained and nanocrystalline structure of B2-phase (Ref 17).

In Fig. 12, maximum completely recoverable strain (Fig. 11) and the number of cycles to failure (Fig. 7) are plotted as functions of PDA temperature and aging time. It can be noted that the higher the annealing temperature, the greater



the recovery strain, but the lower the number of superelastic cycles to failure: The longest strain-controlled fatigue life is observed after PDA at 400 and 450 °C (Fig. 12a). Furthermore, as previously shown (Fig. 7j), 300 °C (1 h) aging results in an almost 20 times increase in fatigue life and smaller maximum completely recoverable SM strains as compared to PDA at 500 °C without aging. Both residual strain-hardening (low-temperature annealing) and  $\omega$ -phase precipitation (aging) phenomena increase the material yield stress (Ref 13). As a result, in the low-temperature annealed and aged samples, at the same testing temperature (RT), the accumulated plastic deformation is smaller and superelastic fatigue life is longer. On the contrary, strain- and precipitation-induced hardening decrease the quantity of martensite formed and reoriented at  $-196$  °C (SM testing strain-inducing temperature) and therefore recovered upon heating of deformed samples.

## 6. Conclusions

1. For Ti-19.7Nb-5.8Ta (at.%) alloy, annealing at 500–600 °C after moderate cold rolling ( $e = 0.37$ ) results in the formation of a nanosubgrained structure in  $\beta$ -phase as a result of polygonization of a dislocation substructure. After annealing at 650–750 °C, recrystallization and grain growth occur. A distinct lamellar contrast in TEM images after annealing at 500 °C can be attributed to  $\alpha'$ -martensite crystals formed during cooling and thin foil preparation at  $-38$  C.
2. Low-temperature aging (300 °C) of the  $\beta$ -phase nanosubgrained structure is accompanied by the  $\omega$ -phase precipitation phenomena. Up to 1 h of aging,  $\omega$ -particles preserve their globular shape, random distribution, and very fine size. During further aging, elongated rows of coarsened  $\omega$ -particles form.
3. Depending on the annealing temperature, the studied alloy manifests either mainly superelastic or mainly shape memory behavior at RT: PDA under 500 °C results in mainly superelastic behavior, whereas PDA at 500 °C and higher results in mainly shape memory behavior; the maximum completely recoverable SM strain is observed after CR (0.37) + PDA (600–700 °C), and its value is close to 2%.
4. As compared to unaged alloy, an “optimum”  $\omega$ -phase precipitation hardening caused by 300 °C, 1-h aging of the nanosubgrained substructure resulting from CR ( $e = 0.37$ ) + PDA (500 °C, 1 h) leads to a more than 20 times longer cyclic life.
5. Both the well-developed dislocation substructure obtained after CR ( $e = 0.37$ ) + PDA (400/450 °C, 1 h) and the precipitation-hardened nanosubgrained microstructure obtained after CR ( $e = 0.37$ ) + PDA (500 °C, 1 h) + aging (300 °C, 1 h) result in similar fatigue lives, but the aged alloy appears to be much more ductile than the simply annealed one.

## Acknowledgments

The present work was carried out with the financial support of the Natural Science and Engineering Research Council of Canada and of the Ministry of Education and Science of the Russian Federation.

## References

1. I.J. Stevens, J. Alexander, Bone Implant, U.S. Patent 3579831, Issued 1971-05-25
2. G.C. Leventhal, Titanium: A Metal for Surgery, *J. Bone Joint Surg.*, 1951, **33**, p 473–474
3. C. Baker, The Shape-Memory Effect in a Titanium-35 wt.% Niobium Alloy, *Met. Sci. J.*, 1971, **5**, p 92–100
4. K. Takamura, K. Hayashi, N. Ishinishi, T. Yamasda, and Y. Sugioka, Evaluation of Carcinogenicity and Chronic Toxicity Associated with Orthopedic Implants in Mice, *J. Biomed. Mater. Res.*, 1980, **28**(5), p 583–589
5. M. Long and H.J. Rack, Titanium Alloys in Total Joint Replacement—A Material Science Perspective, *Biomaterials*, 1998, **19**, p 1621–1639
6. M.I. Petrzhiik, S.G. Fedotov, U.K. Kovneristiy, and N.F. Zhebyneva, Влияние термоциклирования на структуру закаленных сплавов системы Ti-Ta-Nb (Influence of Thermocycling on the Structure of Quenched Ti-Ta-Nb Alloys), *Met. Sci. Heat Treat. Met.*, 1992, **3**, p 2–4 (in Russian)
7. S. Miyazaki, H.Y. Kim, and H. Hosoda, Development and Characterization of Ni-Free Ti-Base Shape Memory and Superelastic Alloys, *Mater. Sci. Eng. A*, 2006, **438–440**, p 18–24
8. H.Y. Kim, Y. Ikehara, J.I. Kim, H. Hosoda, and S. Miyazaki, Martensitic Transformation, Shape Memory Effect and Superelasticity of Ti-Nb Binary Alloys, *Acta Mater.*, 2006, **54**(9), p 2419–2429
9. V. Brailovski, S. Prokoshkin, M. Gauthier, K. Inaekyan, S. Dubinskiy, M. Petrzhiik, and M. Filonov, Bulk and Porous Metastable Beta Ti-Nb-Zr(Ta) Alloys for Biomedical Applications, *Mater. Sci. Eng. C*, 2011, **31**, p 643–657
10. M. Geetha, A.K. Singh, A.K. Gogia, and R. Asokamani, Effect of Thermomechanical Processing on Evolution of Various Phases in Ti-Nb-Zr Alloys, *J. Alloys Compd.*, 2004, **384**, p 131–144
11. V. Brailovski, Stress-strain Diagrams, Chapter 6, *Shape Memory Alloys: Fundamentals, Modeling and Applications*, V. Brailovski, S. Prokoshkin, P. Terriault, and F. Trochu, Ed., ÉTS, Montréal, 2003, p 844
12. V. Brailovski, S. Prokoshkin, K. Inaekyan, S. Dubinskiy, and M. Gauthier, Mechanical Properties of Thermomechanically-Processed Metastable Beta Ti-Nb-Zr Alloys for Biomedical Applications, *Mater. Sci. Forum*, 2012, **706–709**, p 455–460
13. E.W. Collings, *The Physical Metallurgy of Titanium Alloys*, ASM, Metals Park, 1984, p 223
14. K. Otsuka, C.M. Wayman, Mechanism of Shape Memory Effect and Superelasticity, Chapter 2, *Shape Memory Materials*, K. Otsuka, and C.M. Wayman, Ed., Cambridge University Press, 1998, p 284
15. S.M. Dubinskiy, S.D. Prokoshkin, V. Brailovski, A.V. Korotitskiy, K.E. Inaekyan, M.R. Filonov, and M.I. Petrzhiik, Structure Formation During Thermomechanical Processing of Ti-Nb-Zr(Ta) Alloys and Manifestation of the Shape-Memory Effect, *Phys. Met. Metall.*, 2011, **112**, p 529–542
16. U. Krupp, *Fatigue Crack Propagation in Metals and Alloys: Microstructural Aspects and Modeling Concepts*, Wiley, New York, 2007, p 287
17. A. Kreitsberg, V. Brailovski, S. Prokoshkin, Y. Facchinello, K. Inaekyan, and S. Dubinskiy, Microstructure and Functional Fatigue of Nanostructured Ti-50.26at%Ni Alloy After Thermomechanical Treatment with Warm Rolling and Intermediate Annealing, *Mater. Sci. Eng. A*, 2013, **562**, p 118–127